

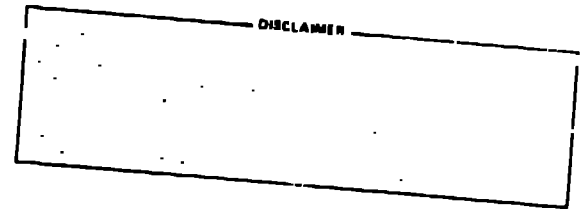
**MASTER**

CONF-80-128--1

**TITLE:** INTENSE ELECTRON-BEAM PROPAGATION IN LOW-DENSITY GASES USING PHERMEX

**AUTHOR(S):** David C. Moir, Barry S. Newberger, Lester E. Thode

**SUBMITTED TO:** JOWOG 6, SNLA, Albuquerque, New Mexico



University of California

By acceptance of this article, the publisher recognizes that the U.S. Government retains a nonexclusive, royalty-free license to publish or reproduce the published form of this contribution, or to allow others to do so, for U.S. Government purposes.

The Los Alamos Scientific Laboratory requests that the publisher identify this article as work performed under the auspices of the U.S. Department of Energy.

DISTRIBUTION OF THIS DOCUMENT IS UNLIMITED



**LOS ALAMOS SCIENTIFIC LABORATORY**

Post Office Box 1663 Los Alamos, New Mexico 87545

An Affirmative Action/Equal Opportunity Employer



INTENSE ELECTRON-BEAM PROPAGATION  
IN LOW-DENSITY GASES USING PHERMEX

By

David C. Moir, Barry S. Newberger, and Lester E. Thode

ABSTRACT

Preliminary propagation experiments have been performed using the LASL-PHERMEX 21-MeV electron beam with current densities of 40 kA/cm<sup>2</sup>. Gas densities are varied from 10-m torr to 580 torr. Results indicate the presence of microinstabilities.

---

I. INTRODUCTION

Significant interest persists, both here<sup>1</sup> and abroad,<sup>2</sup> in the technology development of intense charged particle beams and propagation of such beams through plasma formed in neutral gas by the beam itself. Due to the substantial source of free energy represented by the drift energy of the beam, propagation could be plagued by a variety of well-known macroinstabilities and microinstabilities, e.g. hose,<sup>3</sup> kink,<sup>4</sup> two-stream<sup>5-7</sup>, and filamentation.<sup>8-10</sup>

Because of the complex, time-dependent interplay between plasma generation and collective instabilities, it is essential that time-resolved propagation experiments in the 20-60 MeV be conducted to provide a baseline for theory, in order that reliable scaling laws can be established. In this regard, near-term technology development of the existing PHERMEX standing-wave linac<sup>11</sup> would provide a device for answering a

number of fundamental issues concerning endoatmospheric, ultra-relativistic electron beam propagation. PHERMEX has an intrinsic high repetition rate and multiple-pulse capability, and thus a number of propagation scenarios could be investigated.

## II. PHERMEX AS AN INTENSE ELECTRON BEAM SOURCE

PHERMEX is an acronym for Pulsed High Energy Radiographic Machine Emitting X-rays. The facility consists of a 50 MHz standing-wave linear electron beam accelerator housed in a blast-proof building. The pulsed 20-30 MeV electron beam is focused on a tungsten target to produce a bremsstrahlung radiation spectrum, which is used for flash radiography of exploding systems.<sup>11</sup>

The original facility was built between 1957 and 1963, and until recently has been used almost exclusively for flash radiography in weapon and weapon-related programs. Use of the PHERMEX facility for electron beam experiments has only recently been considered. The following factors have been important in this decision:

- A. Slight reduction in the hydrodynamic shot schedule,
- B. Increased reliability of the linear accelerator,
- C. Upgrade of detection chamber fast electronics, and
- D. Interest in extending the basic physics of intense electron beams.

The PHERMEX accelerator parameters are summarized in Table I. The first column refers to the present parameters and the second to the parameters after an upgrade program which is in progress and scheduled for completion in late FY 1981. A schematic drawing of the accelerator with the important elements is shown in Fig. 1.

TABLE I

INJECTOR (HOT CATHODE)	<u>Today</u>	<u>Post-Upgrade</u>
Voltage (MV)	0.550	1.00-1.25
Current (A)	350	650
Pulse Width (ns)	200, 100, 40	150, 80, 40
Risetime (ns)	50, 40, 15	13, 13, 13
RF Synchronized	No	Yes
Emittance (nm-mrad)	< 500 $\pi$	< 500 $\pi$
Spotsize (mm)	25	25
RF CAVITIES		
Frequency (MHz)	50	50
Length (m)	2.6	2.6
Diameter (m)	4.6	4.6
Field Strength (MV/m)		
$\alpha$	3.6	12.0
$\beta$	5.5	10.0
$\gamma$	3.4	8.0
Stored Energy (J)		
$\alpha$	610	6800
$\beta$	1430	4700
$\gamma$	550	3000
Energy Depletion ( $\alpha$ -cavity)		
One Micropulse	6%	3%
Ten Micropulses	30%	20%

Electrons are generated on a hot-cathode injector. The cathode is pulsed by a high-voltage pulse and electrons are accelerated and focused into  $\alpha$ -cavity. The present injector system consists of a 10-cm diameter sintered tungsten-barium oxide impregnated cathode which operates at 1100° C. The surface emits 6-8 A/cm<sup>2</sup>. At present, the cathode is pulsed by a 500 kV Femcor pulser which determines the macroscopic time structure of the beam. Various pulse widths in Table I are attained by physically changing pulser units. The Femcor pulsers are not synchronized to the 50 MHz rf of the accelerating cavities because the time jitter of the output pulse ( $\pm 30$  ns) is significantly larger than the time between two successive accelerating cycles. In addition, the risetime for both the 200 ns and 100 ns pulses is larger than the accelerating period.

The Femcor pulser will be replaced by a three pulse 1 MV system constructed by Physics International (PI). The projected increase in current is due to the increased voltage of the pulser. However, it is limited by the maximum emission capability of the hot cathode. The PI pulser is capable of generating one, two, or three pulses (each approximately 40 ns in duration) completely merged or separated by delays of up to 30  $\mu$ s. PI has tested delays between pulses up to 100  $\mu$ s and larger delays may be possible but are as yet untested. The output pulse has low jitter ( $\pm 8$  ns) and a fast risetime and it will be synchronized with the 50 MHz rf.

The microscopic time structure of the beam is produced by the accelerating cycles of the 50 MHz rf which occur every 20 ns. The first cavity ( $\alpha$ ) acts as a chopper and accelerator with substantial stored energy depletion in that cavity. The micropulses generated by rf acceleration are approximately gaussian with a 3.3 ns FWHM. The number and

amplitude of the micropulses in a macropulse is clearly dependent on the injected pulse shape and timing relative to the rf. Figure 2 is a time resolved measurement of the electron beam current for a 200 ns pulse on the injector from the Femcor pulser. Note that a sub-burst with maximum current does not occur until the third pulse. This phenomena is a function of pulse risetime and jitter relative to the rf. At present, the initial conditions for a full amplitude pulse are unknown and determined by the initial low intensity pulses. Installation of the PI 1-MV pulser, which will be synchronized with the rf, will yield an initial sub-burst of full amplitude. This upgrade is significant for electron beam experiments.

PIERMEX has three rf cavities shown schematically in Fig. 1. These are designated  $\alpha$ ,  $\beta$ , and  $\gamma$ . The beam is injected into  $\alpha$ . The field strength in the cavities is generated by rf amplifiers. As part of the upgrade, the existing amplifiers are being replaced with amplifiers of higher power. As a consequence, the field strengths and stored energy in the cavities will be greatly increased.

Electron beam energy is determined by the strength of the cavity fields. The beam energy and other output beam parameters are summarized in Table II. Beam energy dispersion and emittance have been determined by calculation using beam spot size measurements at two locations in the drift space, a field map of the final focusing lens, and the beam spot size at the focus.

As noted earlier, the time structure of the output beam is determined macroscopically by the injection pulse and microscopically by the 50 MHz rf. These parameters are also summarized in Table II.

Figure 3 is a glass plate measurement of the PHERMEX electron beam distribution at the focus. The white spot is due to a threshold effect in the radiation damage of the glass plate. The diameter of the white spot is assumed to be the beam spot size. However, radiographic techniques used to determine beam spot size indicate a slightly smaller value.

The beam current measurement, shown in Fig. 2, and spot size, indicated in Fig. 3, can be combined to determine the peak current density and electron density in individual micropulses. These values are also summarized in Table II. It should be noted again that these values are for a single micropulse of maximum amplitude.

As also noted earlier, the support electronics associated with PHERMEX have been upgraded. This upgrade substantially enhances our capability to perform time-resolved electron beam experiments. Table III is a summary of the presently available electronics. This particular phase of the upgrade program is essentially complete.

It is useful to compare PHERMEX with other machines in terms of relativistic factor  $\gamma$ , current, current density, pulse duration and total beam energy. This comparison is given in Table IV. At present, PHERMEX is the only high  $\gamma$  machine in operation. The current density is sufficiently high that beam-plasma effects are important. However, the peak current and total energy are somewhat low in comparison with what is considered optimum for beam propagation. On the other hand, with 3 kA of beam current, combined with the existing multiple pulse capability, PHERMEX would represent a powerful and versatile device for investigating ultrarelativistic, endoatmospheric beam propagation.

TABLE II

	<u>Today</u>	<u>Post-Upgrade</u>
MEAN ENERGY (MeV)	21	40
ACCESSIBLE ENERGY RANGE (MeV)	20-30	20-60
ENERGY DISPERSION	4%	4%
EMITTANCE (mm-mrad)	7 $\pi$	7 $\pi$
<b>TIME STRUCTURE</b>		
Macropulse Width (ns)	200, 100, or 40	150, 90, or 40
Risetime (ns)	51, 37, 15	13, 13, 13
Number of Micropulses	10, 5, 2	7, 4, 2
Micropulse Width (ns)	3.3 (FWHM)	3.3 (FWHM)
<b>INTENSITY</b>		
Average over Macropulse (A)	50 (200 ns)	90 (150 ns)
Peak (kA)	0.30	0.60-0.80
Electrons/Micropulse	$6 \times 10^{12}$	$1.2 \times 10^{13}$
Current Density (Peak) (A/m <sup>2</sup> )	$4 \times 10^8$	$8 \times 10^8$
Electron Density (Peak) (e/m <sup>3</sup> )	$4 \times 10^{18}$	$8 \times 10^{18}$
<b>SPOT SIZE (DIAMETER)</b>		
Exit of Collimating Lens (mm)	15	15
Entrance to Focusing Lense (mm)	10	10
On Target with 0.5 m focus (mm)	$\leq 1$	$\leq 1$

TABLE III

## COMPUTER

Data General, 80 k Memory, 10 M byte disc, 9 track tape unit,  
floppy disc, Versatech printer, 2-Camac crates.

## TRANSIENT ANALYZERS

Tektronix R-7912, 11 channels, 250 MHz bandwidth

Biomation 8100, 6 channels, 25 MHz bandwidth

Tektronix Oscilloscopes, 5, 50 MHz bandwidth

## TIMING CHANNELS

Nanofast, 20 channels, 0.1 ns resolution,  $\pm 1$  ns accuracy,  
200  $\mu$ s total range

Nanofast, 10 channels, 10.0 ns resolution,  $\pm 10$  ns accuracy,  
10 s total range

TABLE IV

	$\gamma$	$I$ (kA)	$J$ (kA/cm <sup>2</sup> )	$\tau$ (ns)	$U$ (J)
FX-25	2.9	15.0	4.8	30.0	600
PI 1590	13.0	100.0	15.0	60.0	40000
ASTRON	7.8	0.10	0.13	300	120
ETA	4.8	10.0	60	30.0	1500
PERMEX	41	0.30	40	3.3	200*
PERMEX (post-upgrade)	41-121	0.60-0.80+	80	3.3	280-1130*
ATA	98	10.0	60	30	15000

$\gamma$  = electron energy/electron rest mass

$I$  = electron beam current

$J$  = current density (peak)

$\tau$  = pulse length of individual pulses

$U$  = total beam energy ( $U = I\tau \times$  number of micropulses)

\* PHERMEX generates multiple pulses

+ present development effort

### III. PRELIMINARY PROPAGATION EXPERIMENTS

In order to demonstrate the feasibility of using PHERMEX as an intense electron beam source, some beam characterization and preliminary propagation experiments were performed.

Figure 4 is a drawing of the basic experimental arrangement for all of the electron beam studies. All experiments were performed external to the building on the PHERMEX firing point. The electron beam is focused through a tapered beryllium collimator, and exits through a 0.25-mm thick beryllium window. A new section of drift tube was inserted through the existing accelerator bullnose from the outside. This new drift tube contains a  $1.3 \times 10^{-2}$  mm kapton vacuum window, which is located 7 mm from the beryllium window. Thus, a 7 mm air gap, which has a negligible effect on the beam, exists between the two drift spaces. For this configuration, the position of the 1 mm diameter beam focus is located about in the center of the air gap.

Initial experiments were directed toward characterizing the PHERMEX electron beam. The first experiment was a time-resolved current measurement in vacuum using a graphite charge collector located 50 cm from the 1 mm focus. The results of this experiment are shown in Fig. 2 and were discussed in Section I.

In an attempt to further unfold the beam distribution function, the beam momentum scatter was varied by placing additional scattering foils in the gap between the beryllium and kapton vacuum windows. High-resolution glass photographic plates (Kodak S0343) were then used to measure the beam spatial distribution at 60 cm from the beam focus. For propagation in vacuum, the densitometer scans of the beam spatial

distribution for various added scattering materials are shown in Fig. 5. As expected, the increased beam scatter produced a measurable, systematic change in the spatial distribution function. To zero order, the particle trajectories are ballistic because the PHERMEX beam has a  $v/\gamma \sim 3.8 \times 10^{-4}$ . Here, we use conventional notation:  $v = Nr_e$ , where  $N$  is the number of the beam electrons per unit length,  $r_e$  is the classical electron radius, and  $\gamma$  is the relativistic factor. For the photographic plate data, the integrals of the distributions are normalized to be the same.

In Fig. 6, the beam divergence calculated on the basis of the beam spatial distribution, with systematic beam divergence subtracted out, is compared with what would be predicted by Molière multiple scattering theory.<sup>21</sup> The experimental errors are dominated by the uncertainty in the systematic beam divergence, which has been calculated to be about  $\theta_{div} \sim 20$  mrad. However, the systematic divergence has not been measured directly. From these data, the random angular scatter in the beam momentum distribution is in good agreement with theory.

The beam distributions in Fig. 5 show no evidence of structure. From this result and spot size at the focus, an estimate of the co-linearity of the micropulses can be derived. Spatially, the micropulses are separated by less than 1 mm at the focus. The maximum angular separation is less than 5 milliradians.

The first set of time integrated data was beam distribution measurements normal to the PHERMEX beam. The detectors for these measurements were glass plates. They were positioned 60 cm from the 1 mm focus. Figures 7a and 7b are a compilation of the results. The plates are arranged as a function of nitrogen gas pressure (row) and increasing

beam scatter (column). The distribution indicates that beam instabilities are present and decrease with both increasing beam scatter and gas pressure at a position 60 cm from the beam focus.

Open shutter photographs were made of the beam propagating through neon and helium. A lucite drift tube was attached to the end of the metal drift tube, as shown in Fig. 4. Figures 8a and 8b contain the results of measurement for neon and helium, respectively. The beam is propagating from left to right with the extreme left being located 60 cm from the focus. The results at low pressure for both gases show the possible existence of a two-stream instability. This is evidenced by the bright glow of the gas near the entrance into the lucite drift tube. At higher pressures, the beam is breaking up into filaments. The transverse distribution is consistent with what is seen in the normal distribution, measured by glass plates. To verify that these effects were not produced by discontinuities in the return-current path, open shutter photographs were made with the lucite drift tube lined with copper wire screen. The photographs indicated that the return-current discontinuity had no visible effect.

To understand the effect of the beam microstructure, time-resolved measurements were made of the beam propagating in neon and helium. Time resolved measurements of the normal and transverse beam distribution were made using an IMACON 790 fast-frame/streak camera. The camera was able to record a 10 ns frame every 50 ns. Figure 9 is a reproduction of normal beam distribution for a beam propagating in 3 Torr of neon. The numbered overlay relates the images to appropriate beam micro-pulses. Cherenkov light produced by electrons passing through a thin plastic sheet was used

to generate light for the images. It is located 1.9 m from the focus. Synchronization of the camera relative to the micro-pulses was determined using the NanoFast time digitizer and is shown in the schematic below the picture. Photographs were also taken of the transverse beam distribution where the light was generated by the gas itself. The following conclusions can be reached from these measurements: (1) the micropulses propagate independently, and (2) there is no light emitted from the gas during the 20 ns between pulses. Note, however, that no ultraviolet light is transmitted through the lucite drift tube.

A segment of the metal drift tube was constructed which contained magnetic-field (B) probes. It was attached to the end of the drift tube used in previous experiments. Figure 10 is a photograph of this section. A kapton window was placed on the downstream end. The charge collector was attached to the end of the drift tube. Figure 11 is a diagram of the entire arrangement. The charge collector was maintained at vacuum, and the return-current probes were located in a region of variable pressure. The purpose of this arrangement was to isolate the charge collector from any electron plasma currents which might be produced in the gas by the electron beam and impinge on the charge collector.

The drift tube contained a bellows on the upstream end. This was used to align the beam on the center of the drift-tube axis. The drift tube and the charge collector were maintained at vacuum, and each of the beam probes was checked using separate beam pulses. The resulting integrated signals agree to within two standard deviations of the observed pulse-to-pulse dispersion of beam current. Probe signals were connected to a passive adder which summed the outputs and generated a

signal that was proportional to the net current traveling through the spool containing the probes.

A series of measurements was made of the net current in the gas versus the total current in the charge collector for both neon and helium. Figure 12a is a measurement of the integrated probe output for the beam propagating in vacuum. Figure 12b is the same measurement with the beam propagating through 10  $\mu$  of helium. This result indicates that after seven micropulses, the gas is sufficiently ionized that the return-current is now in the beam-generated plasma and no longer in the drift-tube wall. Figure 12c is for 1 atmosphere of helium, and the measured probe return currents which are again in the drift tube as in the vacuum case. However, the slopes are substantially different. For the first pulse, the net current is substantially larger than the actual beam current as measured by the charge collector. It is speculated that this additional current is produced by beam-generated delta rays. Figure 13 is a plot of the ratio of the net current measured by the probes to the total current measured by the charge collector as a function of pressure from vacuum to 580 torr. Between 1.0 and 10.0 torr, the net current measured by the probes is zero, and all of the return current is in the beam-generated plasma. At lower pressures (<1 torr), there is insufficient gas to generate enough plasma to conduct the entire return current. At higher pressure (>10 torr), the electrons from the ionized gas tend to rapidly recombine, thus limiting the conductivity and forcing the return current through the drift tube. The data for neon have similar properties; however, the two curves diverge in the 100-600 torr range with the neon return current being systematically lower. Unfortunately, the data

cannot be systematically analyzed using the initial micropulse because the slow risetime and time jitter of the pulser yield initial pulses of varying amplitude.

#### IV. SUMMARY

In this paper, we have described our preliminary experiments carried out to examine the potentiality of using the LASL PHERMEX facility as a device to explore the physics of relativistic electron beam transport in neutral gas.

These experiments yielded substantial evidence for the existence of some kind of beam-plasma instability. Since the beam was propagated over distances less than a betatron wavelength, we are led to conclude that this instability must be of the type often referred to as microinstability rather than a macroscopic mode as, for example, the hose instability.

## REFERENCES

1. "Particle Beams, Laser Weapons-1." Aviation Week & Space Technology, (July 28, 1980), 32-42.
2. "Soviets Build Directed-Energy Weapon," Aviation Week & Space Technology, (July 28, 1980), 47-50.
3. Edward P. Lee, "Resistive Hose Instability of a Beam with the Bennett Profile," Phys. Fluids 21, 1327 (1978).
4. Edward P. Lee, "Low-Frequency Hydromagnetic Kink Mode of a Relativistic Beam," Phys. Fluids 16, 1072 (1973).
5. M. M. Shoucri and A. B. Kitsenko, "Oscillations of Bounded Beam-Plasma Systems in a Cylindrical Geometry," Plasma Physics 10, 699 (1968).
6. B. S. Newberger, "Relativistic Electron Beam Propagation: Two-Stream Theory January 1978-January 1979," Los Alamos Scientific Laboratory Report LA-7912-MS (July 1979).
7. B. S. Newberger and L. E. Thode, "Two-Stream Instability for a Scattered Beam Propagating in a Collisional Plasma," Proceedings of Third International Conference on High-Power Electron and Ion Beam Research and Technology, Novosibirsk, USSR (July 1979).
8. R. Lee and M. Lampe, "Electromagnetic Instabilities, Filamentation, and Focusing of Relativistic Electron Beams," Phys. Rev. Lett. 31, 1390 (1973).
9. K. Molvig, C. W. Roberson, and T. Tajima, "Surface Filamentation of Relativistic Electron Beam in a Plasma," Phys. Fluids 21, 975 (1978).
10. T. Okada and K. Niu, "Collisional Effects in the Electromagnetic Instability for a Relativistic Electron Beam Penetrating a Plasma," Institute of Plasma Physics Report IPPJ-439, Nagoya University, Japan (February 1980).
11. D. Venable et al., "PIERREX: A Pulsed High-Energy Radiographic Machine Emitting X-Rays," Los Alamos Scientific Laboratory Report LA-3241 (May 1967).
12. H. A. Bethe, "Molière's Theory of Multiple Scattering," Phys. Rev. 89, 1256 (1953).

## FIGURE CAPTIONS

- Figure 1 Schematic diagram depicting the important elements of the PHERMEX standing-wave linear accelerator.
- Figure 2 Charge-collector voltage versus time for the PHERMEX electron beam measured at 50 cm downstream of the 1 mm focus. Peak (negative) voltages correspond to 0.27 kA of current.
- Figure 3 Photograph of a radiation-damaged glass plate located at the focus of the PHERMEX beam relative to centimeter scale. The white spot is due to a threshold effect in the radiation damage process.
- Figure 4 Electron beam experimental arrangement and PHERMEX bull-nose. The beam is focused through the beryllium collimator to a 1-mm-diameter spot between the beryllium vacuum window and kapton window.
- Figure 5 Densitometer scans of the radiation damage spot produced in glass by the beam at 60 cm from the 1 mm focus. The curves are normalized to unit area. The beam is transported in vacuum from the focus after passing through thin foils of different material and thickness, as illustrated. The respective rms diameter is also shown.
- Figure 6 Experimentally determined mean scattering angles as a function of the calculated values from small angle multiple scattering theory. The dashed curve is  $\theta_{exp} - \theta_{cal}$ . The vertical error bars denote the uncertainty in the inherent beam divergence  $\theta_{div}$ , while the horizontal error bars denote limits in the range of approximations in the theory.
- Figures 7a and 7b Photographs of radiation-damaged glass plates for different values of ambient nitrogen gas pressure (horizontal) and beam scatter (vertical). Gas pressures are as indicated. Scattering angles are, from top to bottom, 18, 30, 32, 37, and 59 mrad, respectively.
- Figures 8a and 8b Composite of open-shutter photographs of the PHERMEX beam injected into (a) neon, and (b) helium. The lucite drift tube begins 60 cm from the 1 mm focus, and the fiducials are 15 cm apart. The blue glow is Cherenkov light in the lucite.

- Figure 9** Imacon 790 fast frame record of the normal beam distribution 1.9 m from 1 mm focus for propagation in 3 torr neon. The overlay correlates the Imacon images with the beam microstructure. Relative timing was obtained using the NanoFast time digitizer.
- Figure 10** Photograph of drift tube segment containing the magnetic field probes used in the net<sub>2</sub> current measurement. Probe areas are approximately 5 cm<sup>2</sup>.
- Figure 11** Return-current measurement experimental arrangement. The charge collector is isolated by a kapton window to prevent collection of plasma current.
- Figure 12** Net current in the drift tube as measured by magnetic field probes for (a) vacuum, (b) 10 μ helium, and (c) 580 torr helium.
- Figure 13** Ratio of the net current in the drift tube to the total propagated current as a function of pressure. The currents are integrated over the entire 200 ns macropulse.

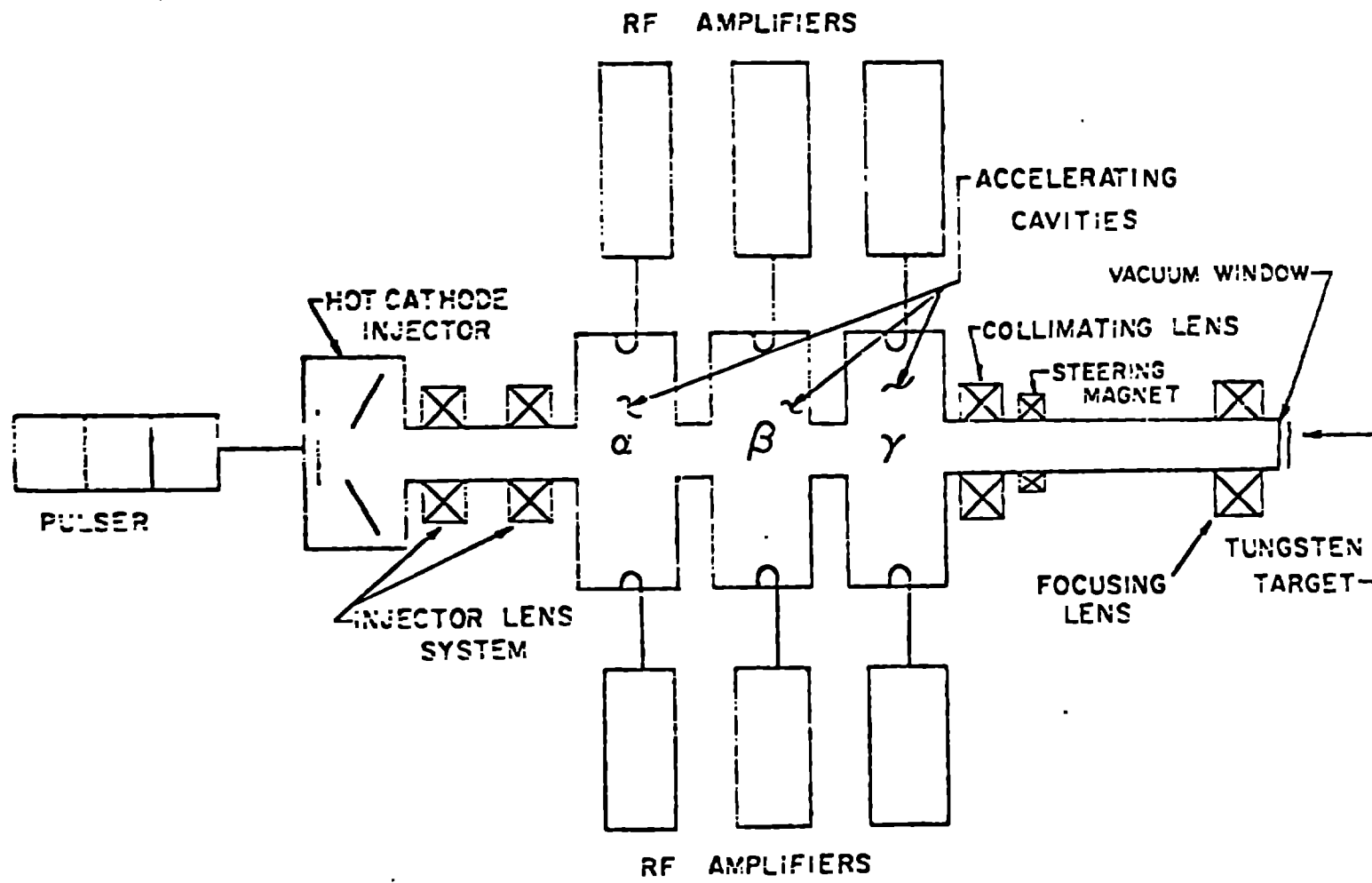


Figure 1

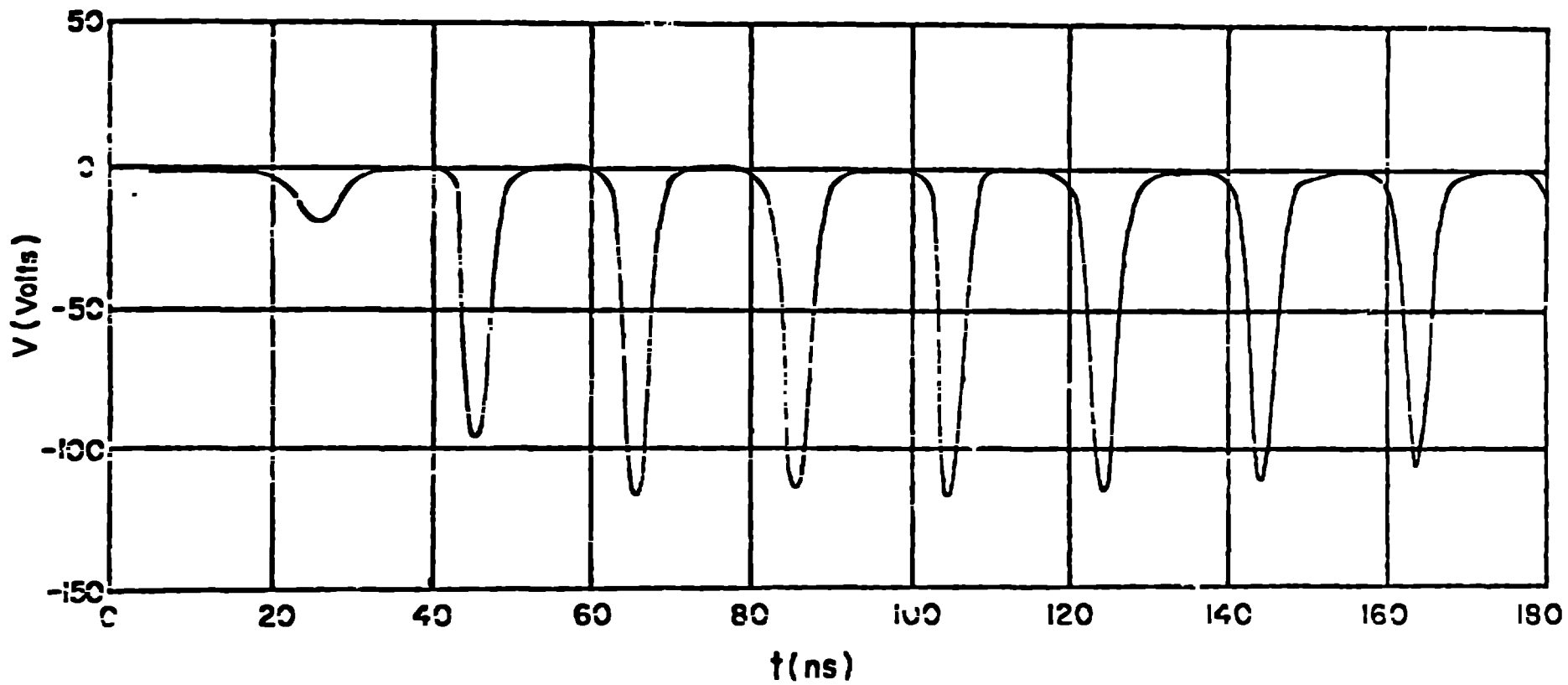


Figure 2

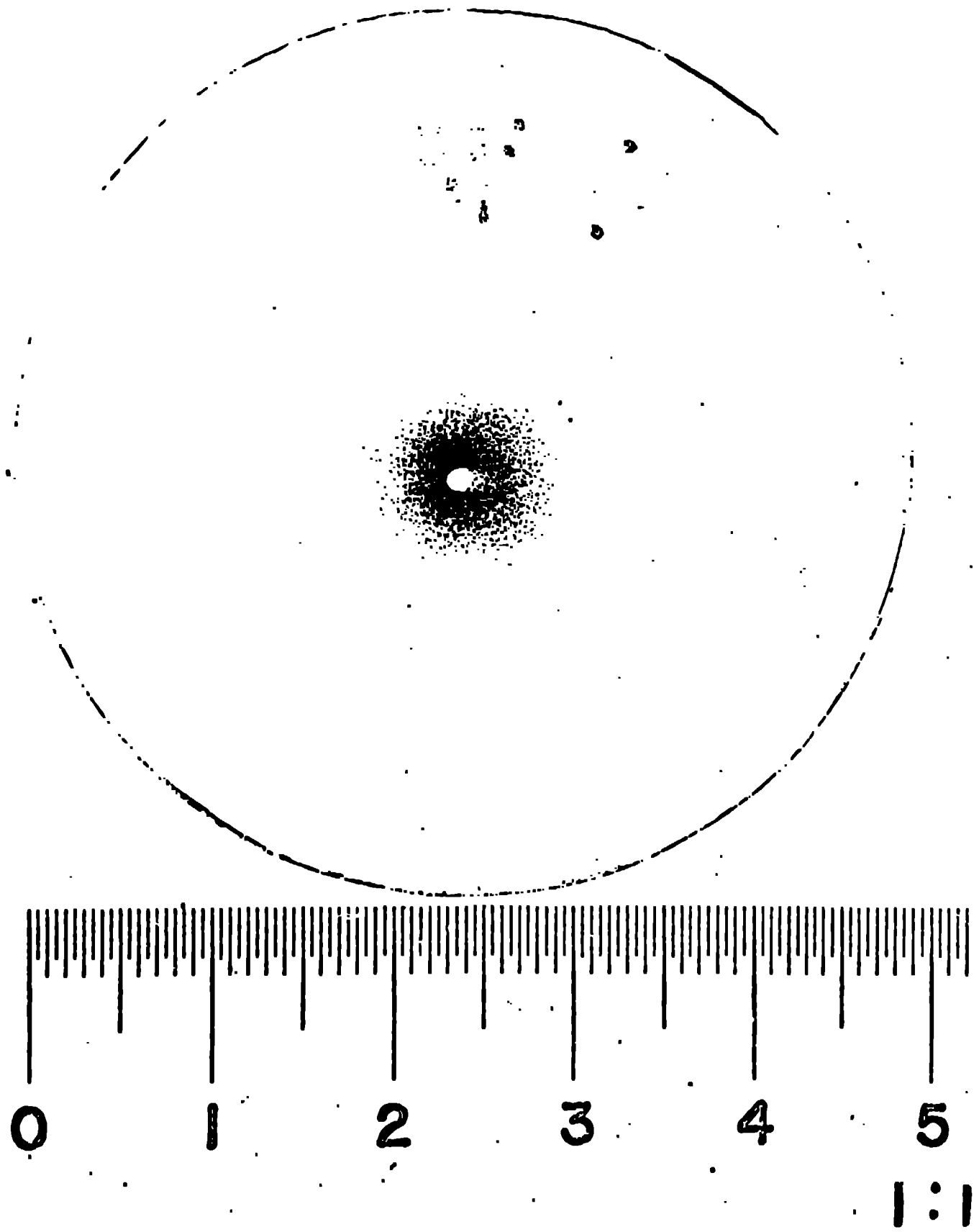


Figure 3

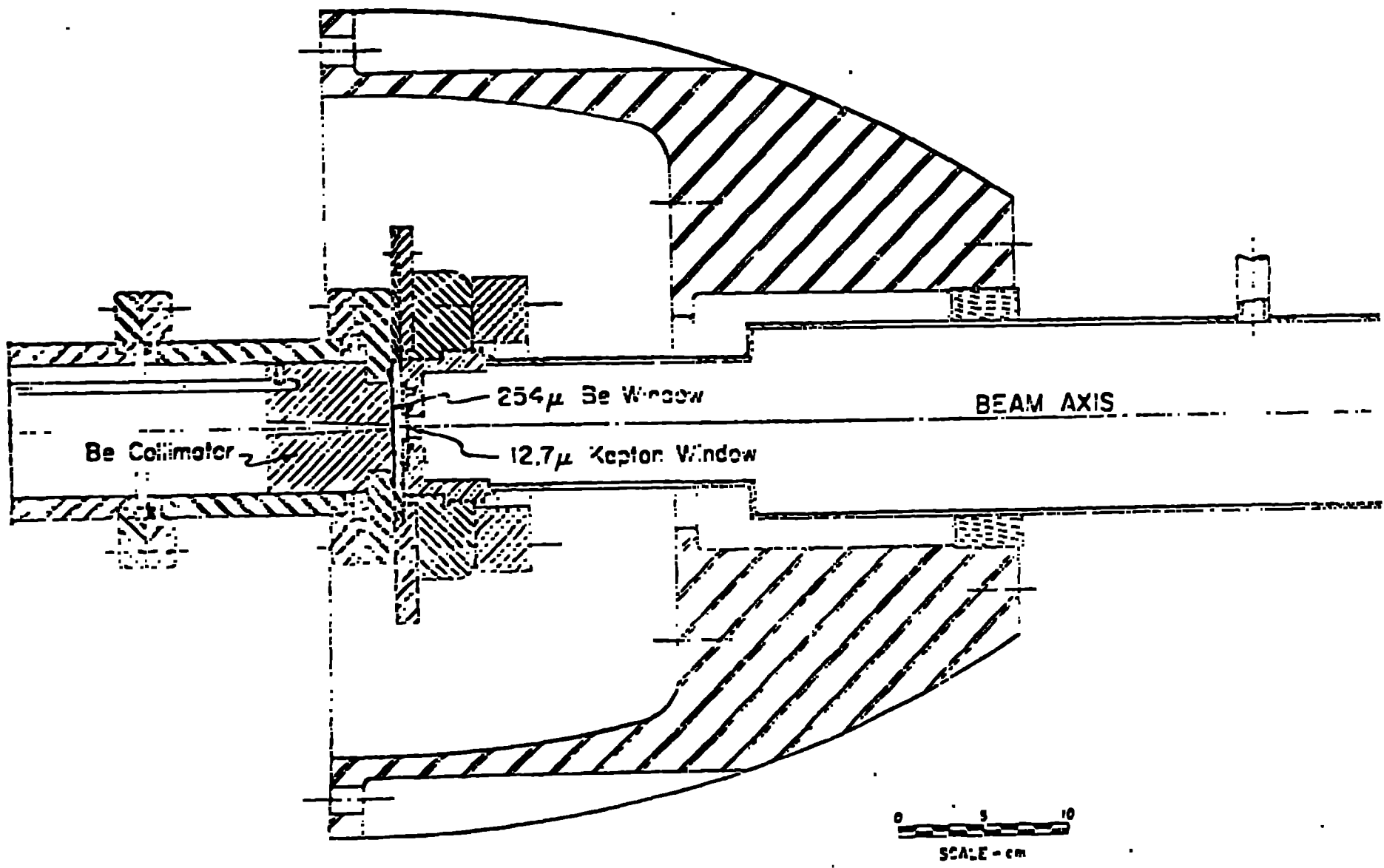


Figure 4

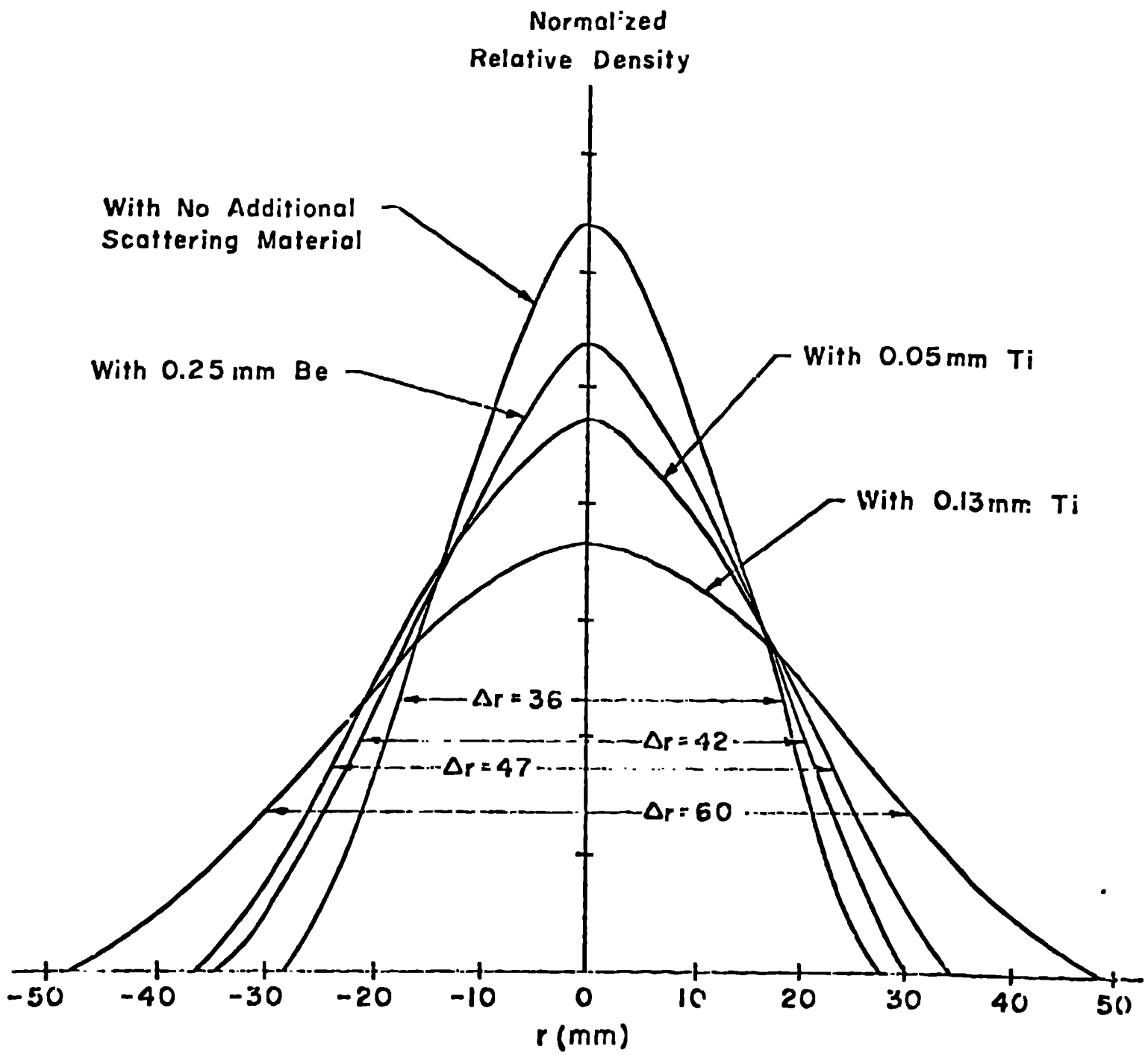


Figure 5

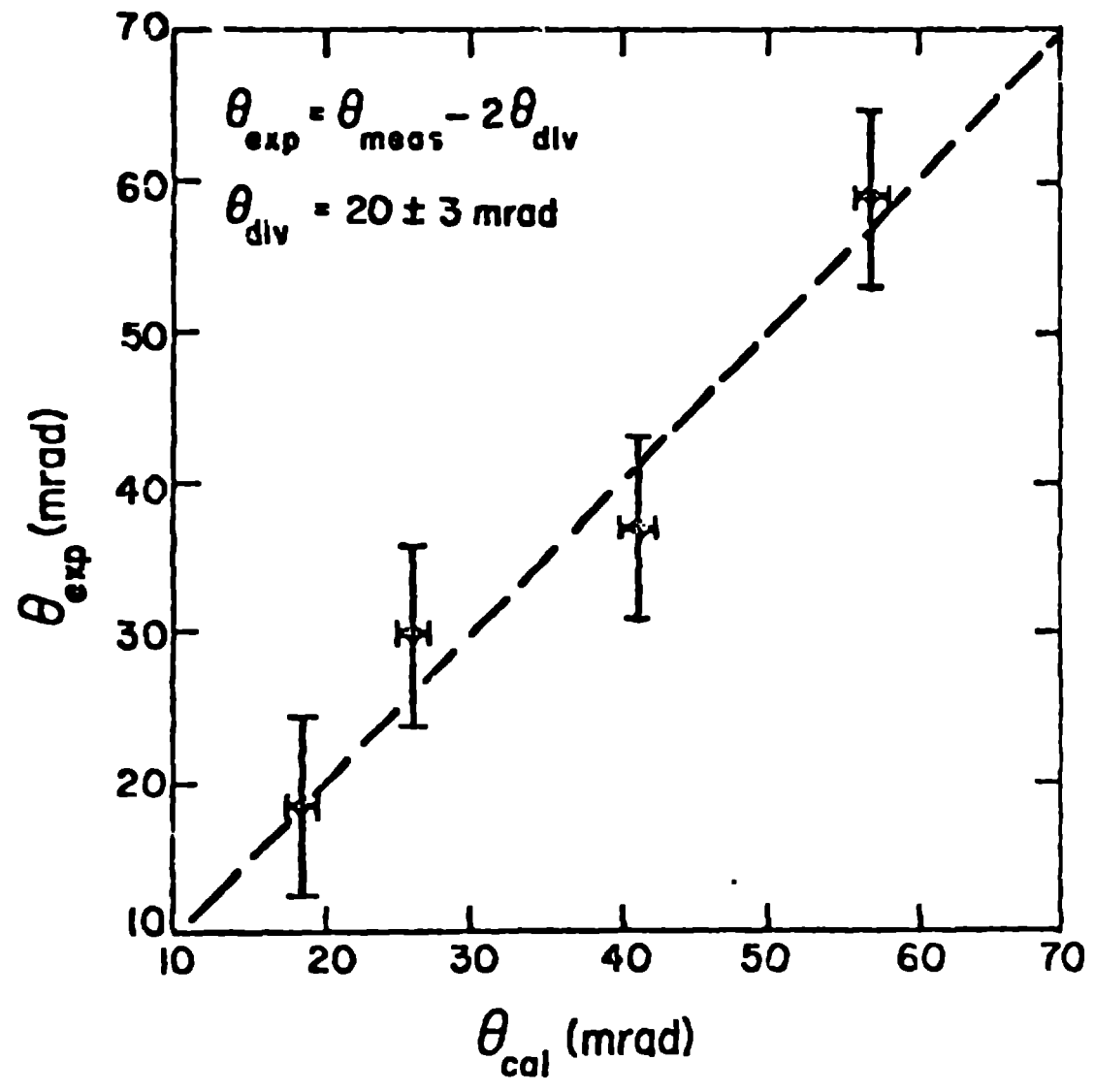


Figure 6

C = No Added Material

A = +10mil Be

B = +20mil Be

E = +2mil Ti

D = +5mil Ti

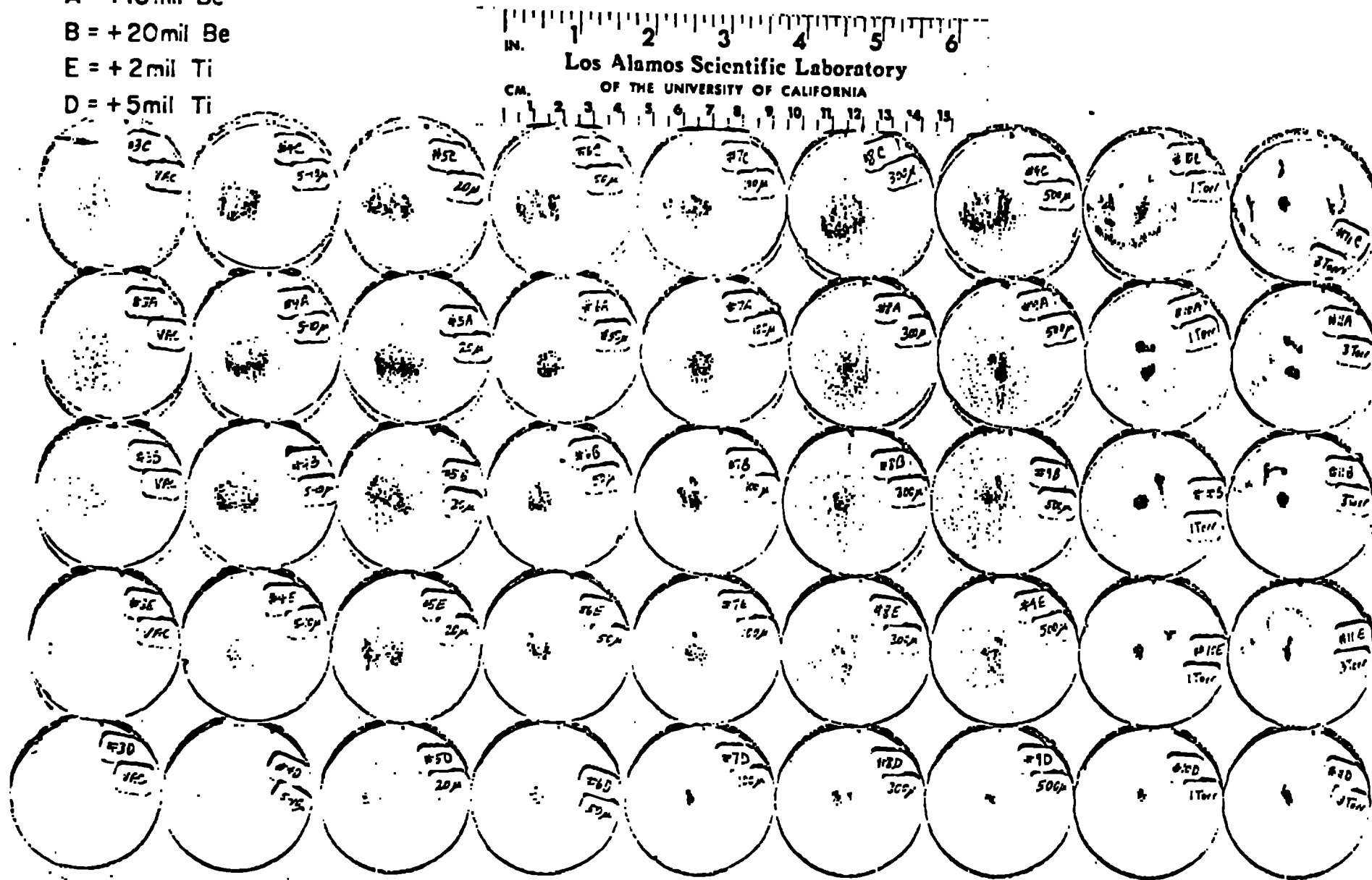


Figure 7a

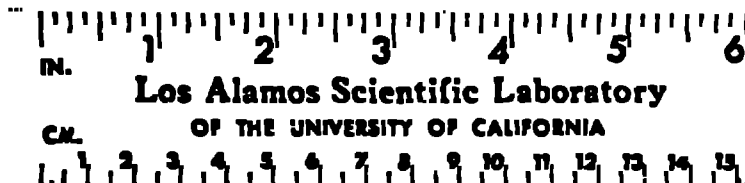
C = No Added Material

A = +10mil Be

B = +20mil Be

E = +2mil Ti

D = +5mil Ti



Los Alamos Scientific Laboratory  
OF THE UNIVERSITY OF CALIFORNIA

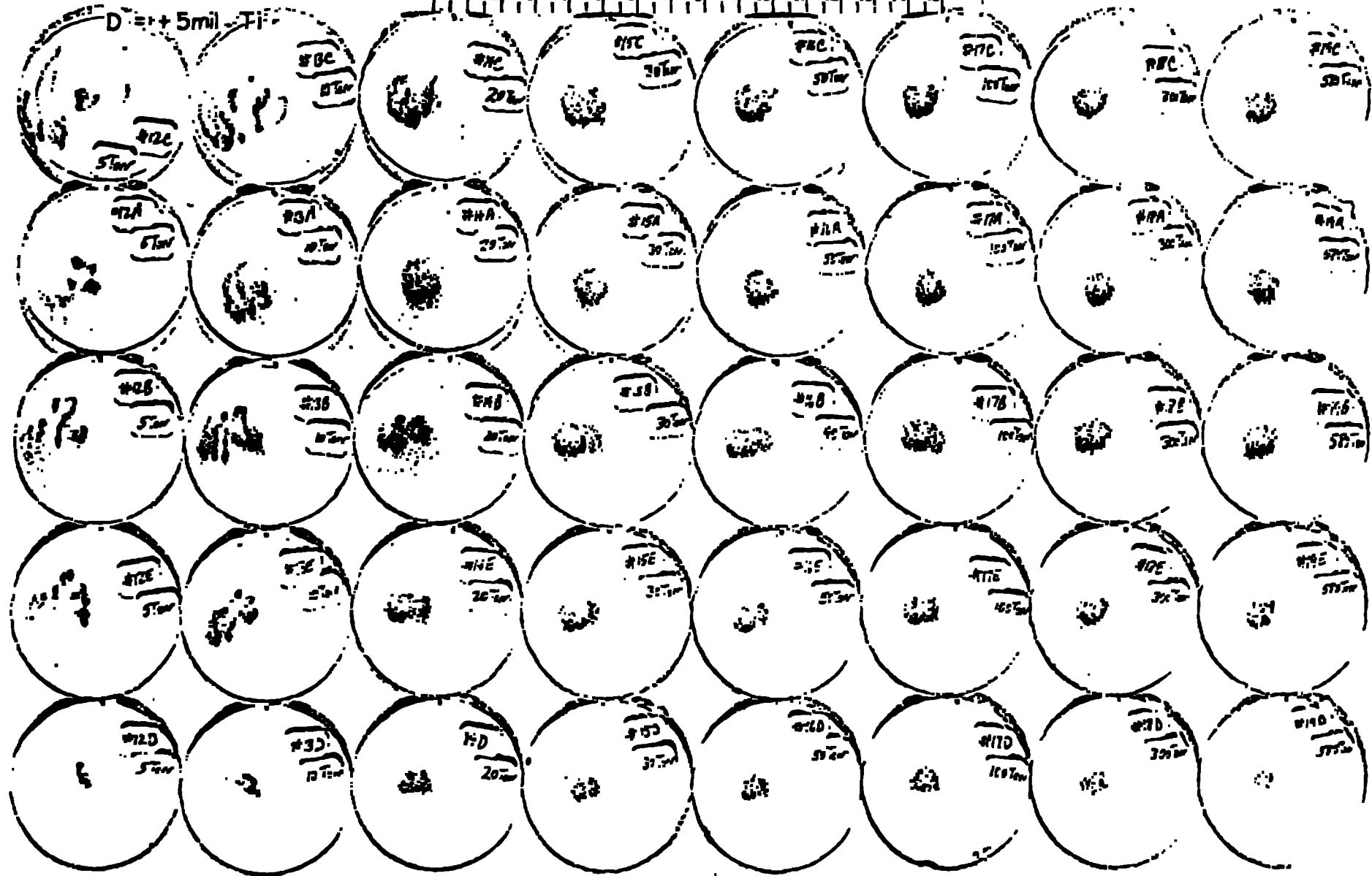
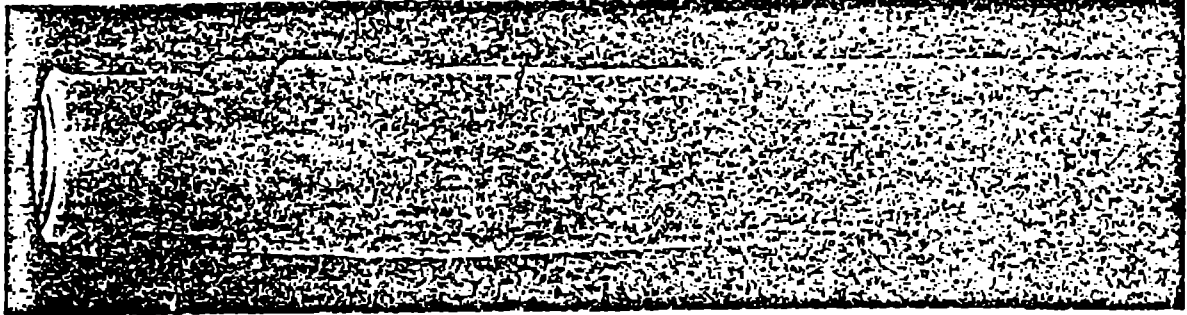
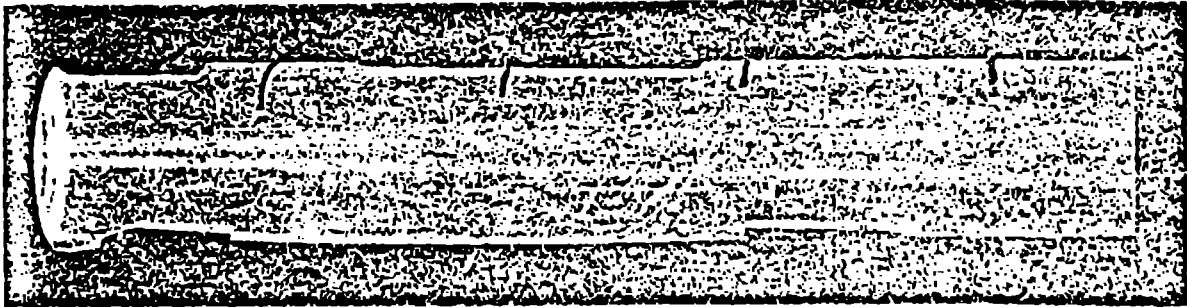


Figure 7b

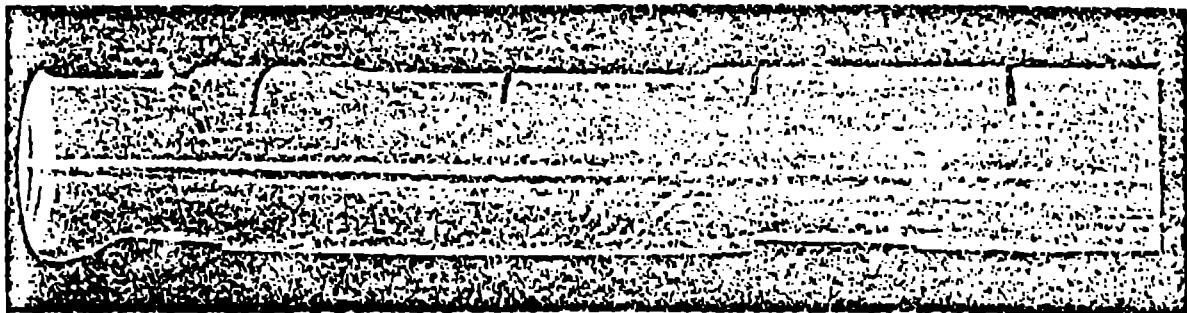
NEON



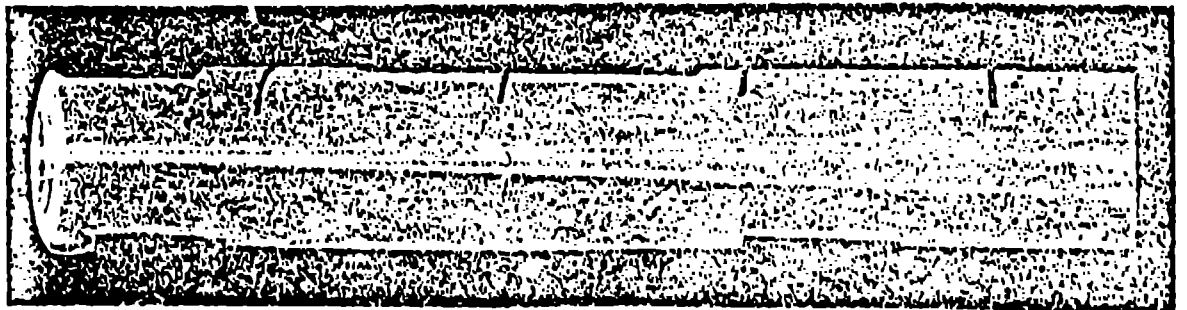
0.3 Torr



3 Torr



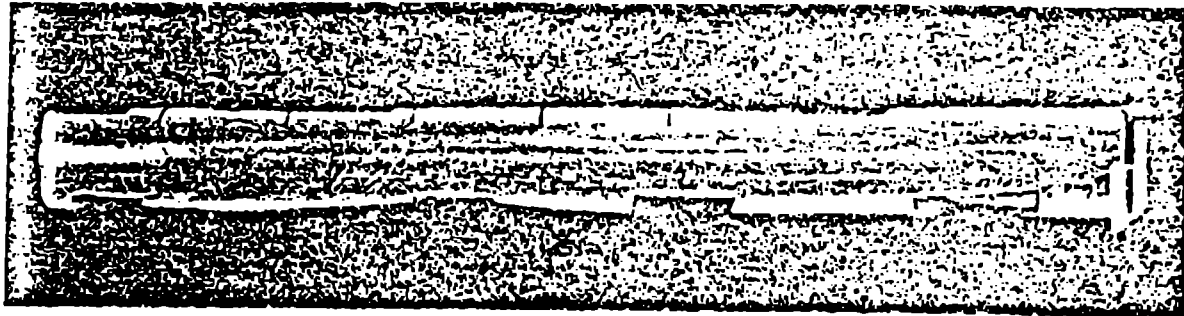
30 Torr



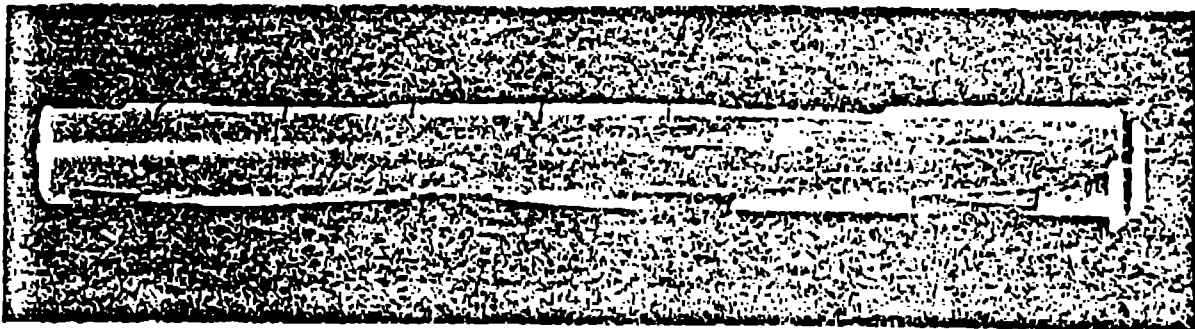
300 Torr

Figure 8a

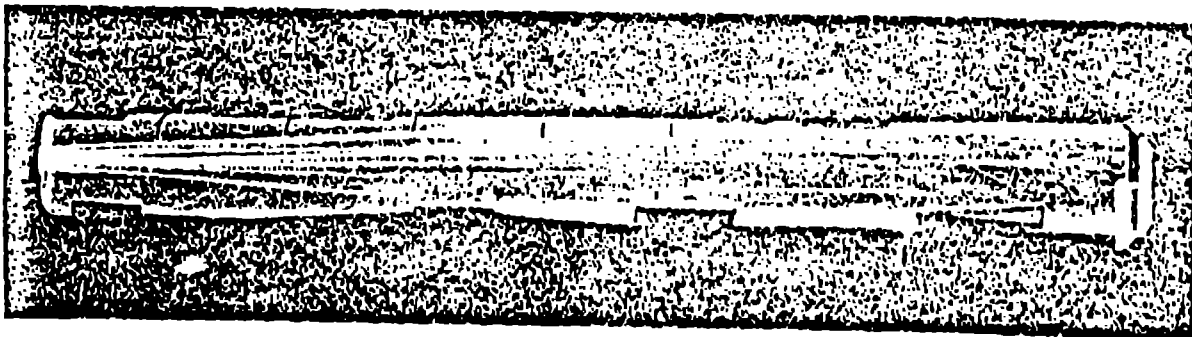
HELIUM



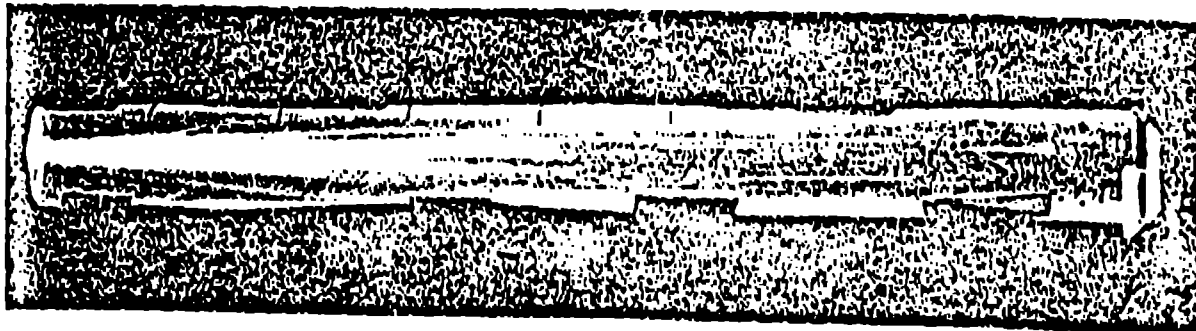
1 Torr



3 Torr



30 Torr



300 Torr

Figure 8b

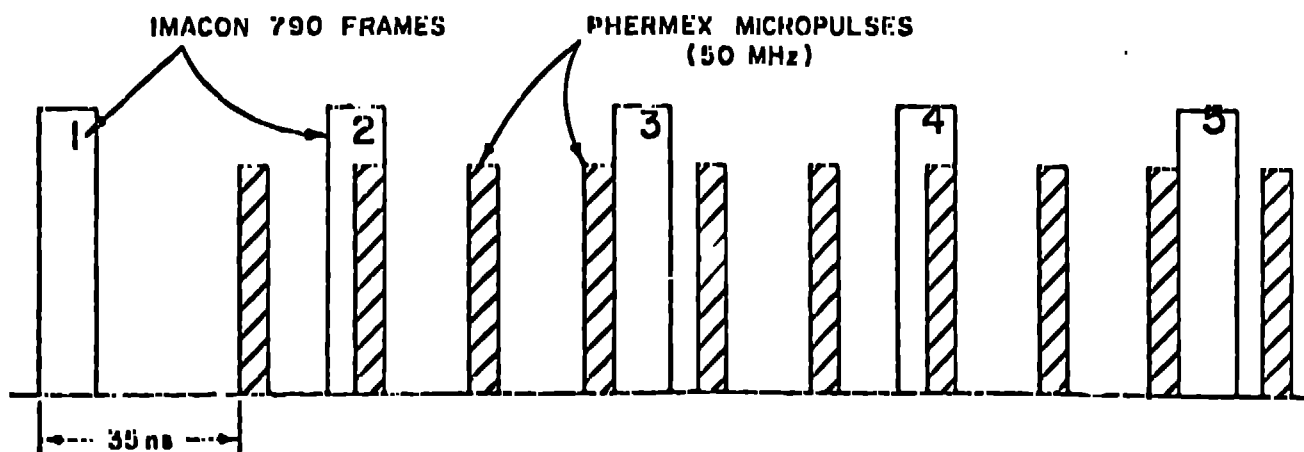
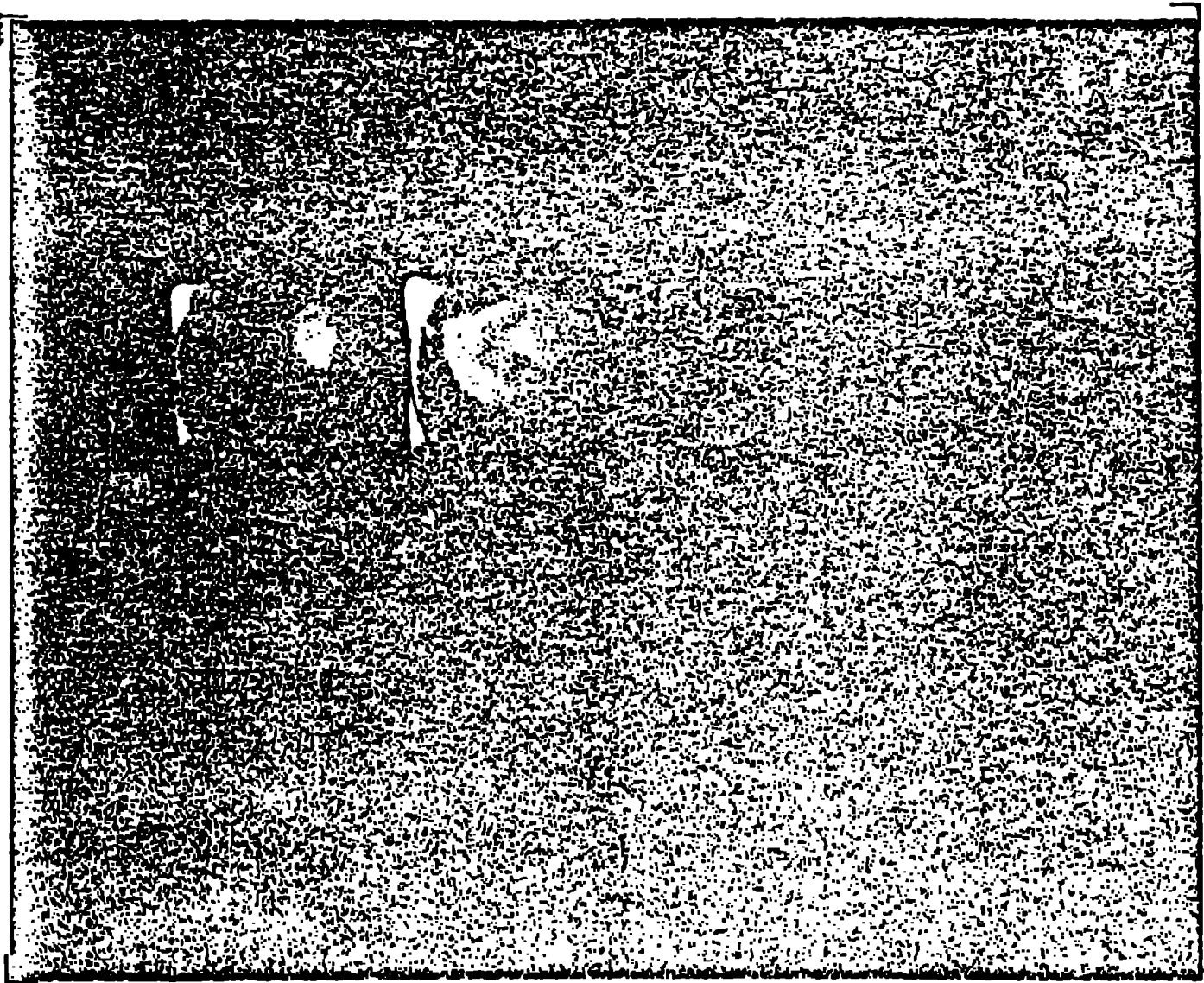


Figure 9

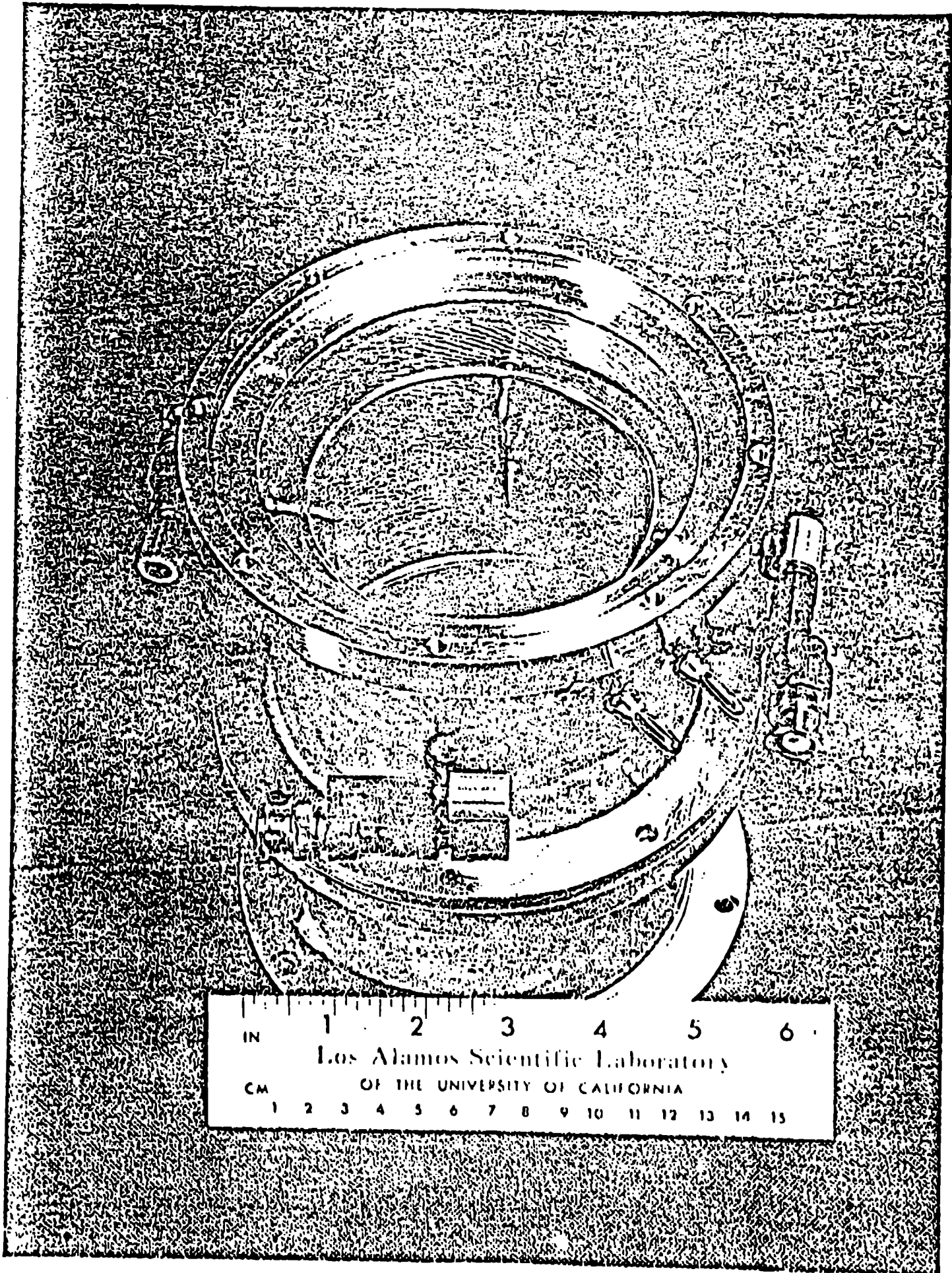


Figure 10

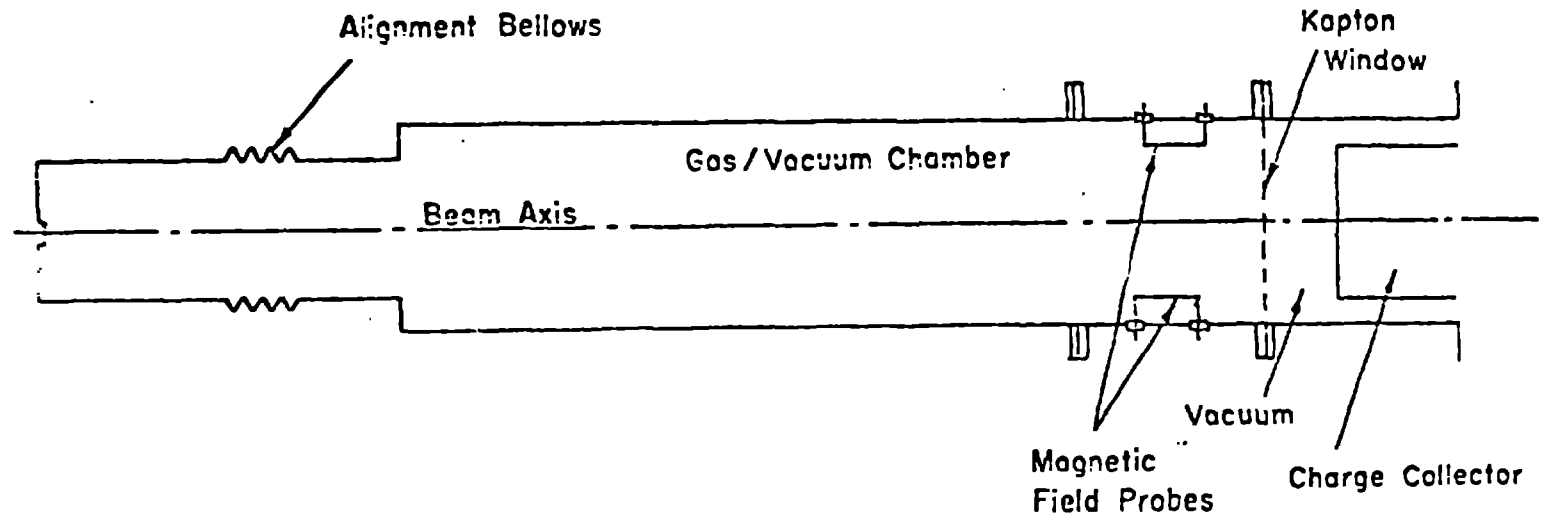


Figure 11

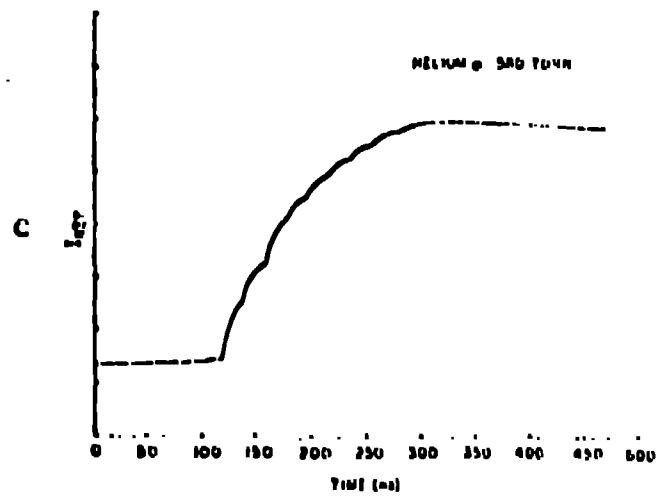
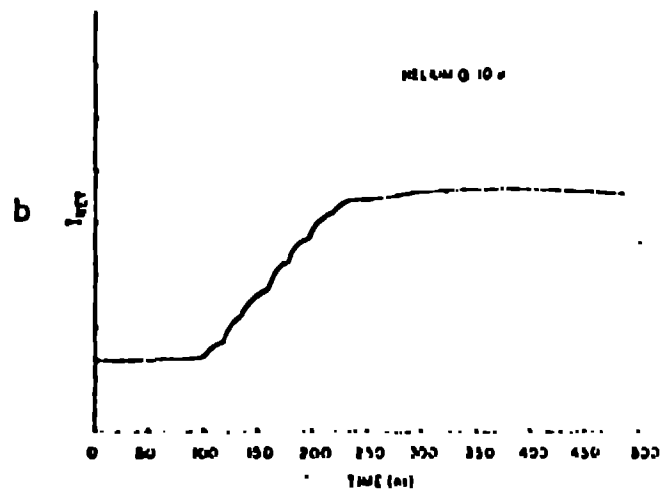
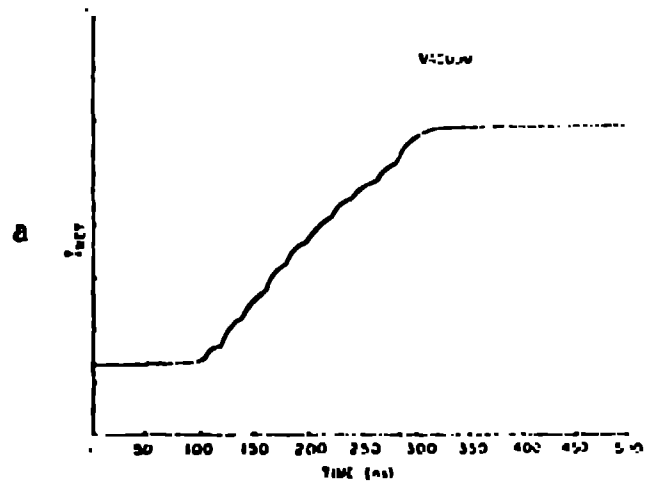


Figure 12

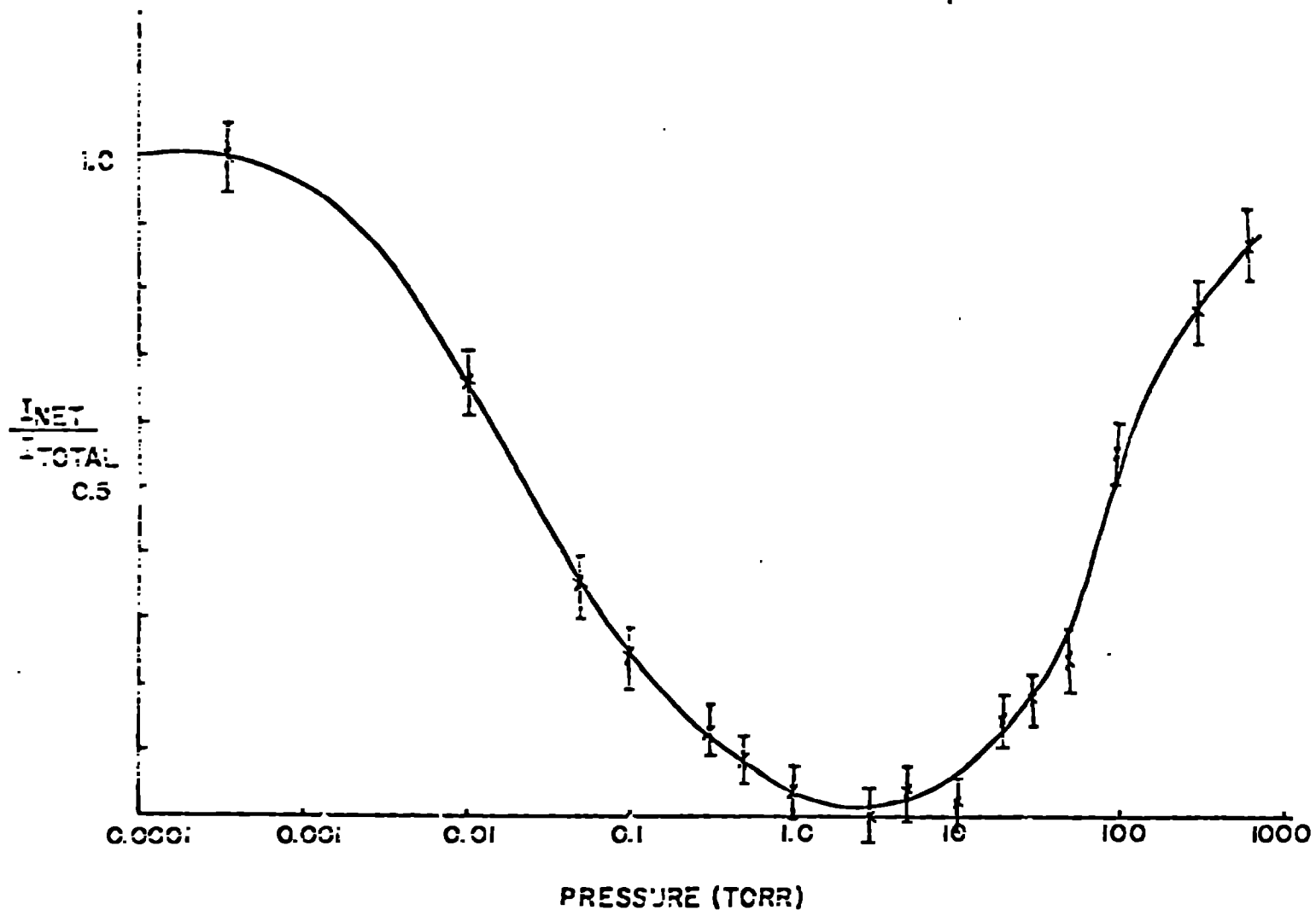


Figure 13